# Data Acquisition, Triggering, and Filtering at the Auger Engineering Radio Array

J. L. Kelley[a], for the Pierre Auger Collaboration[b,1]

[a] *Dept. of Astrophysics / IMAPP, Radboud University Nijmegen, 6500GL Nijmegen, Netherlands*
[b] *Observatorio Pierre Auger, Av. San Martín Norte 304, 5613 Malargüe, Argentina*



**Abstract**

The Auger Engineering Radio Array (AERA) is currently detecting cosmic rays of energies at and above $10^{17}$ eV at the Pierre Auger Observatory, by triggering on the radio emission produced in the associated air showers. The radio-detection technique must cope with a significant background of man-made radio-frequency interference, but can provide information on shower development with a high duty cycle. We discuss our techniques to handle the challenges of self-triggered radio detection in a low-power autonomous array, including triggering and filtering algorithms, data acquisition design, and communication systems.

*Keywords:* radio, cosmic ray, AERA, Pierre Auger Observatory, self-trigger

## 1. Introduction

Cosmic-ray air showers emit coherent broadband radio pulses in the MHz frequency range, a phenomenon discovered by Jelley and collaborators in 1965 [1]. Advances in digital processing technology, along with the potential of the radio technique to determine cosmic-ray primary composition with a high duty cycle [2], have led to renewed interest in the technique [3]. Radio enhancements are now planned at several neutrino and cosmic-ray observatories.

The goals of the Auger Engineering Radio Array (AERA), a 20-km$^2$ extension of the Pierre Auger Observatory in Argentina, are to calibrate the radio signals using hybrid air-shower measurements, and to demonstrate the potential of the technique for future arrays. The first stage of AERA is operational and is successfully measuring air showers of energies at and above $10^{17}$ eV in coincidence with the Auger surface detector (SD) and fluorescence detector (FD) [4].

## 2. Detector and Data Acquisition Design

The first stage of AERA, deployed in September 2010 and July 2011, consists of 24 radio detector stations (RDSs) deployed on a triangular grid with a spacing of 150 m and covering an area of $\sim 0.4$ km$^2$. Each RDS measures the radio signal with a dual-polarization log-periodic dipole antenna (LPDA), aligned north-south and east-west, and sensitive between 27 and 84 MHz. The received signal is further amplified and bandpass filtered, and each polarization is digitized at 200 MHz with 12-bit analog-to-digital converters (ADCs). High-gain (+49 dB after the antenna) and low-gain (+29 dB) versions of each channel are recorded to extend the dynamic range.

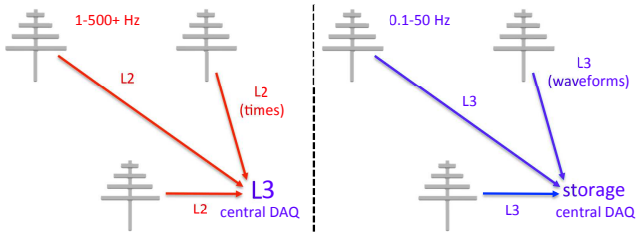


Figure 1: The AERA data flow. The GPS timestamps of station-level triggers (L2) are sent to a central DAQ, which forms multi-station coincidences (L3; shown at left). An L3 request is sent back to the stations (not shown), and digitized waveforms of the event are sent to the central DAQ for storage (shown at right).

A field-programmable gate array (FPGA) in the station electronics forms a trigger when a bandwidth-limited pulse is observed in the voltage traces (a "level 1" trigger). These triggers are passed to a CPU within the RDS, which can then optionally apply other trigger conditions (the "level 2" trigger). The triggers are timestamped using GPS receivers at each RDS.

The CPU in each RDS communicates via Ethernet over a fiber-optic network to a central data acquisition system (DAQ). The RDS reports the trigger timestamps to the central DAQ. The DAQ software forms the "level 3" trigger by using time and spatial coincidences of multiple RDSs, and the time-domain waveform data of these events are requested from each RDS and stored to disk. Figure 1 shows the data flow for each trigger level.

## 3. Triggering and Filtering

Triggering directly on the radio signal of the air showers (instead of using particle detectors as a trigger) poses

*Email address:* j.kelley@astro.ru.nl (J. L. Kelley)
[1]Full author list:
http://www.auger.org/archive/authors_2011_10.html

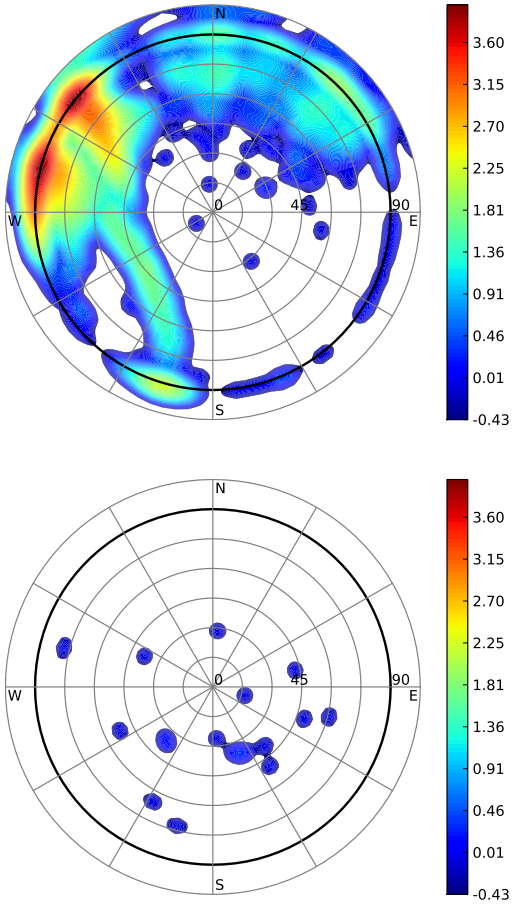


Figure 2: Top: unfiltered AERA polar skymap (2.5h, 40k events). The dark circle indicates the horizon. Bottom: AERA cosmic-ray events coincident with the Auger SD (48d, 18 events). The directions have been smeared with a 3° Gaussian, and the color scale is $\log_{10}$(event density, a.u.).

some challenges for the data acquisition, due to man-made radio-frequency interference (RFI). The continuous background level is set by the radio emission from the Galactic plane, but any man-made narrowband transmitters add to the level above which one must detect air-shower pulses. Additionally, man-made pulsed RFI (from sparking electrical equipment, airplanes, etc.) can mimic the signals from cosmic rays.

A comparison is shown in Fig. 2 between raw level-3-triggered data and self-triggered cosmic-ray events detected in coincidence with the SD. Since the bandwidth and computational resources at each triggering level are limited, one of the technical focuses for the first stage of the array has been to develop various methods to reject RFI in order to minimize efficiency losses from bandwidth saturation.

### *3.1. Narrowband Filtering*

Before triggering on a radio pulse, it is advantageous to increase the signal-to-noise ratio by filtering out any narrowband transmitters from the digitized antenna signals. This is accomplished in a computationally efficient

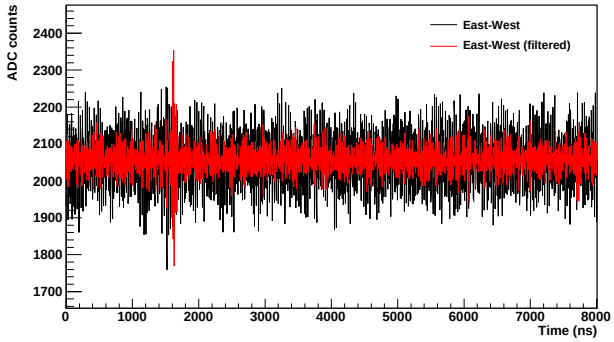


Figure 3: A recorded cosmic-ray radio pulse (at 1500 ns), before IIR narrowband filtering (black) and after (red, pulse offset in time). The peak signal-to-noise ratio increases from 2.4 to 7.6.

manner by using a series of infinite-impulse response (IIR) notch filters in the FPGA. The IIR filters operate on the time-domain signal, and the output of the filter $y_i$ is a linear combination of input samples $x_j$ and delayed feedback output samples $y_j$ from the filter:

$$\begin{aligned} y_i &= x_i - (2\cos\omega_N \cdot x_{i-1}) + x_{i-2} \\ &\quad +(2r\cos\omega_N \cdot y_{i-1}) - (r^2 \cdot y_{i-2}). \end{aligned} \tag{1}$$

The normalized filter frequency $\omega_N$ is given by the notch frequency $f_N$ and the sampling frequency $f_S$,

$$\omega_N = 2\pi f_N / f_S \ , \tag{2}$$

and the width parameter $r$ is a value strictly between 0 and 1, with higher values giving a narrower response function. $r = 0.99$ is typical for a narrow transmitter.

A complication in the implementation of the IIR filters in high-frequency FPGAs arises from the fact that one cannot arbitrarily pipeline the feedback computation. We have resolved this by using the scattered look-ahead pipelining technique [5], which increases the filter complexity but allows more time for computation in the FPGA.

The coefficients of the $x_j$ and $y_j$ in Eq. 1 can be precomputed for the desired notch frequencies, converted to a fixed-point representation, and loaded into the FPGA at run-time. The current design allows for four tunable notch filters for each polarization. See Fig. 3 for an example of the filtering.

An additional filtering technique we are exploring is the use of a frequency-domain median filter. The time-domain signal is first converted to the frequency domain with a fast-Fourier transform (FFT), and then the amplitude of each frequency component $f_i$ is replaced by the median value in a window of size $2N$: $\tilde{f}_i = \text{median}(f_{i-N}, ..., f_{i+N})$. An inverse Fourier transform then converts the signal back to the time domain for triggering. The median filter has the advantage of removing any number of narrowband transmitters, but it is computationally intensive and can distort pulse shapes in the time domain. The pre-trigger FFT also allows for a number of other strategies for signal-to-noise improvement, such as deconvolution of the bandpass filter dispersion, or use of a matched filter [6].

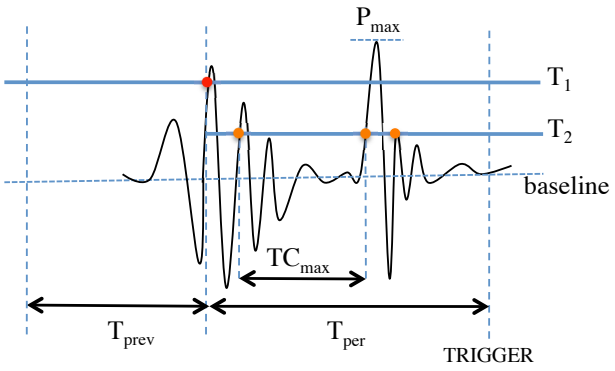


Figure 4: The AERA L1 trigger scheme. See the text for details.

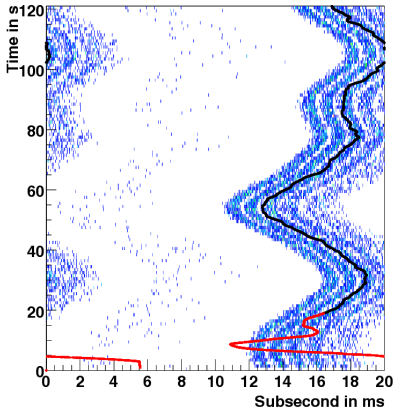


Figure 5: Sample L1 triggers, showing the residual from a 20 ms period (50 Hz) vs. time. The drifting phase can be tracked with a digital PLL (black line).

### *3.2. Level 1 Trigger*

Designed to capture transient, isolated radio pulses, the digitizer uses algorithms in the FPGA to trigger in the time domain on potential signals. At its most basic, the trigger is simply a voltage threshold above a baseline. However, a number of other parameters are added to this trigger to reject RFI. The following trigger conditions are applied to select clean, bandwidth-limited pulses:

1. the voltage rising edge crosses the primary threshold $T_1$;
2. before the $T_1$ crossing, no other $T_1$ crossings occur during the previous time period $T_{\rm prev}$;
3. after the $T_1$ crossing, the signal rising edge crosses a secondary threshold $T_2$, where normally $T_2 < T_1$;
4. the number of rising-edge $T_2$ crossings NC within a time period $T_{\rm per}$ falls within a specified range $\mathrm{NC_{min}} < \mathrm{NC} < \mathrm{NC_{max}}$;
5. the time TC between successive $T_2$ crossings is less than a maximum value $\mathrm{TC_{max}}$;
6. the quotient $Q$ of the pulse maximum $P_{\rm max}$ divided by the number of $T_2$ crossings NC falls within the range $Q_{\rm min} < Q < Q_{\rm max}$ .

The thresholds are compared relative to a baseline voltage, determined dynamically with a rolling average over a specified number of samples. Samples outside of a specified voltage range (i.e. part of a large pulse) are not included in the baseline calculation.

Figure 4 shows the trigger parameters graphically. Each condition is designed to reject man-made RFI with specific characteristics. The quiet period $T_{\rm prev}$ rejects pulse trains. The secondary threshold $T_2$, which is generally set lower than the primary threshold $T_1$, rejects signals with after-pulsing, even if the after-pulsing is weaker than the initial pulse. The condition on the timing and number of $T_2$ crossings allows for some ringing of a bandwidth-limited pulse but rejects long and/or irregular pulse trains or digital spikes. The condition on $Q = P_{\rm max}/\mathrm{NC}$ can select on pulse shape, but in practice this is not needed when the other trigger parameters are set correctly.

Typical values for the thresholds and noise rejection parameters are as follows: $T_1 = 200$ ADC counts and $T_2 = 150$ ADC counts, on an RMS noise level of 40 ADC counts; $\mathrm{NC_{min}} = 1$ and $\mathrm{NC_{max}} = 8$ during a period of $T_{\rm per} = 6.25$ $\mu$s; maximum crossing time $\mathrm{TC_{max}}$ of 130 ns; and a quiet pre-trigger period of $T_{\rm prev} = 1.25$ $\mu$s.

The algorithm can trigger on either signal polarization, or the logical AND or OR of the two. The narrowband filtering described in Sect. 3.1 is performed before the trigger algorithm, but one can also trigger on the unfiltered signal; the unfiltered signal is stored in either case.

### *3.3. Periodicity Filtering*

Man-made pulsed RFI, unlike cosmic-ray air showers, is often periodic in nature. In particular, by examining the time between successive level 1 triggers, clear signatures are visible at 100 Hz and sub-harmonics thereof (twice the power grid frequency of Argentina).

One difficulty in vetoing such events is the drift in phase of the 100 Hz pulses. This can be tracked in the RDS software with the use of a digital phase-locked loop, which can track the changing phase and allow a veto of the periodic events (see Fig. 5).

### *3.4. Directional Filtering*

As shown in Fig. 2, most of the pulsed background events come from man-made sources on the horizon. When a level 3 trigger is formed with three or more stations in coincidence, the DAQ has enough information to reconstruct the direction and veto these events, either with a simple selection on the reconstructed zenith angle, or by using additional azimuthal and timing information. The only limitation is the computation time required for a directional reconstruction, which must keep up with the event rate. A plane-wave fit to the trigger times of the stations is sufficiently fast and accurate for such purposes.

A faster method that can veto directional hot spots, but does not require a full directional reconstruction, uses the distribution of trigger time differences between two stations. Directional hot spots can be identified by peaks

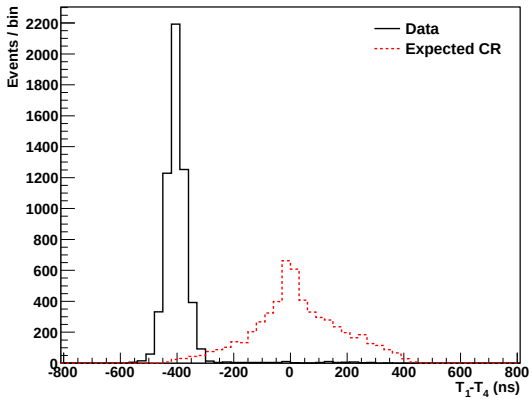


Figure 6: Trigger-time difference between stations 1 and 4 (solid: sample data, showing a pulsed RFI point source; dashed: expected cosmic-ray distribution, normalized to the same number of events).

in the time difference histograms for each station pair, and these distributions are quite different from that expected from air showers (see Fig. 6).

To remove the hot spots, the DAQ forms dynamic histograms $F(i,j)$ of trigger time differences $T_i - T_j$ for each station pair $(i,j)$; the histograms continuously update using a fixed number of past entries. For a candidate level 3 trigger event, the number of "good" time differences $(T_i, T_j)$ is calculated as

$$N_{\rm good} = \sum_{N_{\rm pairs}} \begin{cases} 1 & \text{if } F(T_i - T_j) < F_c \\ 0 & \text{otherwise} \end{cases} , \qquad (3)$$

where $F_c$ is an adjustable threshold that depends on the bin size and number of entries in the histograms. The selection criterion to keep the event is $N_{\rm good} > N_{\rm pairs}/2$ . Future revisions may include the expected time difference distribution of air-shower events as well.

### *3.5. Offline Filtering*

To date, confirmed cosmic-ray events in AERA have been found by searching offline for time coincidences with the water-Cherenkov surface detector of the Pierre Auger Observatory. However, we are developing methods to identify cosmic-ray candidates without information from other detectors.

One promising technique is the use of the signal polarization. Since the primary component of the air-shower radio emission is geomagnetic in nature [7], the direction of the predicted electric field $\hat{e}_g$ is parallel to $\hat{v} \times \hat{b}$, where $\hat{v}$ is the direction of the shower axis, and $\hat{b}$ is the direction of the local magnetic field of the Earth. By deconvolving the response of the antenna and the station electronics, the measured electric field of a radio pulse $\vec{E}(t)$ can be reconstructed [8]. The direction of polarization can be compared to that expected from an air shower with purely geomagnetic emission, i.e., events are selected if

$$\cos^{-1}\left( \hat{e}_g \cdot \frac{\vec{E}_{\rm max}}{|\vec{E}_{\rm max}|} \right) < \Psi_c \ , \qquad (4)$$

where $\Psi_c$ is a threshold space angle. This method does not yet account for the contribution of secondary emission mechanisms with different polarization signatures, such as that from the charge excess in the shower [9, 10]; however, this can in principle be added using additional information such as the core position of the shower.

## 4. Future Plans

AERA will expand in 2012 and 2013 to instrument an area of 20 km$^2$ with 160 radio detector stations. This expansion will entail a transition from communication over optical fiber to a wireless network. Several designs are under development for the wireless system, including:

1. a fully custom time division multiple access (TDMA) system in the 2.4 GHz band that supports up to 180 subscribers per channel, at a bandwidth of 5.5 Mbps;
2. a commercial 802.11n + TDMA system in the 5 GHz band that supports 80-100 subscribers per channel, at a peak bandwidth of 150 Mbps (80 Mbps typical TCP/IP throughput); and
3. a distributed "gossip" protocol in which stations communicate with each other and form multi-station coincidences without communication with a central DAQ.

The first two systems are currently being field tested at the AERA site, while the third system is in the development and simulation stage.

In addition to the developments in data acquisition, triggering, filtering, and communications systems described here, the future stages of AERA will also use enhanced antennas, low-noise amplifiers, and digitization hardware. The increase in efficiency as well as detection area will result in a significant sample of hybrid and super-hybrid events that will be used to quantify the potential of the radio technique for measurement of cosmic-ray air shower energy, direction, and primary composition.

## References

[1] J. V. Jelley *et al.*, Nature **205** (1965) 327-328.
[2] T. Huege, R. Ulrich, and R. Engel, Astropart. Phys. **30** (2008) 96-104; K. D. de Vries *et al.*, Astropart. Phys. **34** (2010) 267-273.
[3] H. Falcke *et al.*, Nature **313** (2005) 313-316.
[4] J. L. Kelley, for the Pierre Auger Collaboration, Proc. 32nd ICRC, Beijing, China, 2011; arXiv:1107.4807.
[5] K. K. Parhi and D. G. Messerschmitt, IEEE Trans. on Acoustics, Speech, and Signal Processing **37** (1989) 1099-1117.
[6] C. Ruehle, for the Pierre Auger Collaboration, Nucl. Instrum. Meth. A **662** (2012) S146-S149.
[7] D. Ardouin *et al.* (CODALEMA Collaboration), Astropart. Phys. **31** (2009) 192-200; W. D. Apel *et al.* (LOPES Collaboration), Astropart. Phys. **32** (2010) 294-303.
[8] P. Abreu *et al.* (Pierre Auger Collaboration), Nucl. Instrum. Meth. A **635** (2011) 92-102.
[9] H. Schoorlemmer, for the Pierre Auger Collaboration, Nucl. Instrum. Meth. A **662** (2012) S134-137.
[10] V. Marin, for the CODALEMA Collaboration, Proc. 32nd ICRC, Beijing, China, 2011.